Nanoscale

PAPER

View Article Online
View Journal | View Issue

Published on 23 May 2014. Downloaded by National Tsing Hua University on 13/08/2015 11:50:24.

Cite this: *Nanoscale*, 2014, **6**, 9034

Simultaneous axial screw dislocation-mediated growth and radial layer-by-layer deposition for controlled synthesis of asymmetric axial ZnO nanospindles†

Hong-Jie Yang, Sheng-Yan He and Hsing-Yu Tuan*

Received 8th April 2014
Accepted 21st May 2014

DOI: 10.1039/c4nr01888e

www.rsc.org/nanoscale

Single-component nanostructures with axial asymmetry were successfully synthesized in organic solvents *via* a new type of growth model. Asymmetric axial ZnO nanospindles with a hexagonal cross-section were produced by a growth model consisting of simultaneous axial screw dislocation-mediated growth and radial layer-by-layer deposition. The growth process of ZnO nanospindles is explained by comprehensively characterizing and monitoring the products at different reaction time intervals. Hexagonal discs containing dislocations were first generated at a reaction time of 2.5 min. When the reaction time continued to increase, the nanodiscs grew along the ⟨0002⟩ direction. Half-nanospindles were formed at mid-reaction stage when the growth rate of [0001] was greater than [000-1]. Finally, the asymmetric nanospindles were obtained at 40 min. Further, the length of the asymmetric axial ZnO spindles can be precisely tuned by the adjustment of reaction temperature. Thus, the growth model presented here can synthesize a new category of one-dimensional asymmetric nanostructures.

Introduction

The vigorous development of nanomaterial synthesis has produced colloidal nanostructures with a variety of sizes, shapes and compositions.[1–6] Highly geometrical symmetric nanostructure is a common structural feature of most colloidal nanostructures.[7–13] Some asymmetric structures (nonspherical shape) have been prepared through a variety of synthetic strategies, such as seed-mediated growth mechanism or surfactant-assisted process, to hinder or accelerate the growth rate of specific crystal planes.[14] For example, one-dimensional nanowires can be produced using Au nanoparticles as seed particles or by the assistance of capping ligands in organic solvents.[15,16] However, the synthesis of single-crystals with single-component asymmetric nanostructures remains a significant synthetic challenge. The key to successful synthesis of less symmetrical nanomaterials is discovering how to break the symmetry of crystal growth to ensure that crystals remain in a highly anisotropic growth, which requires understanding the growth mechanism of nanomaterials for controlling their size and shape.

Zinc oxide (ZnO), an important semiconducting material with a wide band gap (3.37 eV) at room temperature and high exciton binding energy (60 meV), can be used in ultraviolet optoelectronics such as ultraviolet (UV) lasers and transparent conductors.[17–19] ZnO has also been shown to exhibit superior piezoelectric characteristics; it can function as a smart material for piezoelectric device fabrication.[20] Structurally, ZnO has a wurtzite crystal structure and can be described as numerous alternating planes composed of tetrahedrally coordinated O^{2-} and Zn^{2+} ions stacked alternatively along the *c*-axis. This results in two different polar faces along the *c* axis: positively charged (0001), indicating a Zn surface layer, and negatively charged (000-1), indicating an O surface layer, which is surrounded by six nonpolar {10-10} prismatic faces.[21] Probably because of the natural asymmetric hexagonal wurtzite structure and its polar crystal surfaces, ZnO shows a diverse group of nanomaterials.[22] Among various shapes of ZnO nanomaterials, one-dimensional (1-D) ZnO nanostructures in particular have attracted much attention due to their special properties in fabricating nanodevices. A variety of methods for the synthesis of 1-D ZnO nanostructures have been developed, including thermal evaporation, metal–organic chemical vapor deposition, a chemical solution route, hydrothermal synthesis, and electrochemical deposition[23–27] *via* various growth mechanisms, including vapor–liquid–solid (VLS), vapor–solid–solid growth, vapor–solid process, self-catalyzed growth or surfactant assisted process.[28–34] Recently, Jin *et al.* discovered a metal-free 1D nanostructure growth mechanism driven by axial screw dislocation, which was discussed for 1D crystal growth earlier than VLS by Sears in 1955.[35,36] The dislocation-driven nanowire growth mechanism

Department of Chemical Engineering, National Tsing Hua University, 101, Section 2, Kuang-Fu Road, Hsinchu, Taiwan 30013, Republic of China. E-mail: hytuan@che.nthu.edu.tw; Fax: +886-3-571-5408; Tel: +886-3-572-3661

† Electronic supplementary information (ESI) available: XRD pattern, TEM, and SEM images of ZnO nanospindles. See DOI: 10.1039/c4nr01888e

This journal is © The Royal Society of Chemistry 2014

Published on 23 May 2014. Downloaded by National Tsing Hua University on 13/08/2015 11:50:24.

could exist and compete with the VLS mechanism even when the metal seeds were intentionally used to grow nanowires.[37] After that, a series of studies describing dislocation-driven nanowire growth were reported, showing that the mechanism provides a general approach to synthesize several nanomaterials, even for producing nanotubes by alleviating the dislocation strain energy to create a new inner surface.[38–44]

In this study, single component nanostructures with axial asymmetry were obtained by a growth model consisting of two types of growth routes. Asymmetric axial ZnO nanospindles were synthesized in organic solvents at 270 to 370 °C and ~17 MPa. The formation of the asymmetrical axial crystal growth is located at a growth regime where screw dislocation and layer-by-layer (LBL) deposition occur simultaneously; dislocation growth is responsible for the growth of the *c* axis (axial) and LBL deposition is responsible for the growth of the *a*, *b* axis (radial). The length of these nanospindles can be adjusted over a wide range of 0.62 to 4.74 μm. This new growth model provides an effective way for providing a unique shape to colloid nanorods with different degrees of taper; the length of the nanospindle and the tapering situation can be controlled by changing the reaction conditions (temperature and concentration). Thus, the new growth model described here can produce a new category of one-dimensional nanostructures.

Experimental section

Chemicals

All the chemicals were used as received. Zinc acetate ($Zn(Ac)_2$, 99.99%), oleylamine (OLA, 70%), and anhydrous hexane (95%) were purchased from Aldrich.

Synthesis of ZnO nanospindles

To prepare the stock solution of Zn, $Zn(Ac)_2$ (24 mmol) was added to OLA (24 mmol) in a 20 mL glass sample vial. The mixture was degassed with Ar and stirred at 100 °C for 24 h. The color of solution changed gradually to yellow, implying the formation of $Zn(Ac)_2$–OLA complexes. The stock solution was stored in a Ar-filled glove box for further use. Prior to each reaction, Zn stock solution was diluted to an appropriate concentration by adding anhydrous hexane.

In a typical supercritical fluid reaction to produce ZnO nanostructures, 10 mL titanium grade 2 reactor was connected to a high-pressure (1/16″ i.d.) stainless steel tubing *via* a LM-6 HIP (High Pressure Equipment Co.) reducer, loaded with a silicon substrate, heated to 330 °C, and pressurized to 3.4 MPa. The inlet tubing was connected to a six-way valve (Valco) with a 10 mL injection loop, and the titanium reactor temperature was maintained within 1 °C using a temperature controller. Next, the reactant solution was removed from the glove box and injected into the 10 mL injection loop. The precursor solution was injected at a rate of 0.3 mL min^{-1} into the reactor by a high pressure liquid chromatography (HPLC) pump. When the pressure reached 17.2 MPa, the injection flow was turned off and the inlet valve was closed. The reaction was maintained at this temperature for 40 min and the heater was turned off. The reactor was rapidly cooled to room temperature using a cold water bath. Next, the Si substrate was removed from the reactor and all the ZnO nanostructures were collected from the Si wafer. The ZnO nanostructures were purified by centrifugation at 8000 rpm with the addition of 30 mL of toluene for 10 min and repeated three times before further characterization.

Characterization

The crystal structure of the products was obtained by X-ray powder diffraction (Rigaku, Ultima IV X-ray diffractometer) with Cu-Kα radiation operated at 40 kV and 20 mA. XRD samples were prepared by drop-casting the ZnO nanostructures dispersed in hexane onto a glass substrate. The morphology of the ZnO nanostructures was obtained by scanning electron microscope (SEM, Hitachi S-2300) operating at 10 kV or 15 kV accelerating voltage and transmission electron microscopy (TEM) operating by accelerating at 200 kV (JEOL, JEM 2100F) or 300 kV (JEOL, JEM 3000F). For SEM and TEM images, ZnO nanostructures were drop-cast from dispersions in hexane onto silicon substrates and 200-mesh carbon-coated copper grids. The selected area electron diffraction (SAED) patterns of the ZnO nanospindles were also recorded by HRTEM. FTIR spectra were recorded using a Perkin-Elmer Spectrum RXI FTIR spectrometer with 1 cm^{-1} resolution and 64 scans in the range of 4000–400 cm^{-1} by the KBr pellet technique. The ^1H NMR spectra were recorded on a Varian Unity Inova 500 NMR spectrometer using TMS as an internal reference at 25 °C.

Results and discussion

ZnO nanospindles were obtained by the decomposition of the Zn stock solution (100 mM) at an injection rate of 0.3 mL min^{-1} (the molar injection rate of the $Zn(Ac)_2$–OLA complex was 0.03 mmol min^{-1}) at 330 °C and 17.2 MPa in supercritical hexane, which was beyond the critical point of hexane. To study the reaction chemistry of $Zn(Ac)_2$ decomposition mechanism at 330 °C under supercritical hexane, FTIR and NMR spectrometer were performed. It is obvious that $Zn(Ac)_2$ and OLA turn into a yellow clear liquid at 100 °C, indicating that the $Zn(Ac)_2$–OLA complex is formed. By comparing the FTIR (Fig. 1a) and NMR (Fig. 1b) spectra of OLA, $Zn(Ac)_2$–OLA complex and the reaction residue of $Zn(Ac)_2$–OLA complex after synthesis (330 °C), a new peak of the asymmetric stretching mode of C=O group in amide at 1656 cm^{-1} was detected by FTIR at 330 °C, and the other new peak with chemical shift at ~5.8 ppm was assigned to the –CO–NH proton of *N*-oleyl acetamide at 330 °C according to NMR, which indicate that the amide will be generated after heating to 330 °C. According to a previous study, an amine not only acted as a capping ligand but also acted as an attacking agent that attacks the electron-deficient carbon of acetate and undergoes a nucleophilic addition/elimination process to yield ZnO monomers and *N*-oleyl acetamide, as shown in Fig. 1c.[45]

Fig. 2a and b show the SEM images of the as-synthesized ZnO nanospindles on silicon substrates, demonstrating that the products mainly consist of nanospindles randomly oriented on

Published on 23 May 2014. Downloaded by National Tsing Hua University on 13/08/2015 11:50:24.

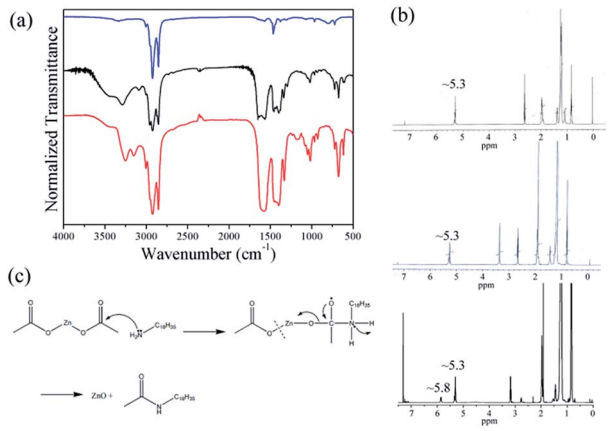

Fig. 1 (a) FTIR spectra for the OLA (blue), $Zn(Ac)_2$–OLA complex (black), and the reaction residue of $Zn(Ac)_2$–OLA complex after heating to 330 °C (red), the solid product was separated by centrifugation. (b) NMR spectra of OLA (upside), $Zn(Ac)_2$–OLA complex (middle), and the reaction residue of $Zn(Ac)_2$–OLA complex after heating to 330 °C (underside). The solid product was separated by centrifugation and $CDCl_3$ was used as the solvent. (c) Illustration of the reaction mechanism of zinc acetate decomposition with oleylamine at 330 °C and 17.2 MPa in supercritical hexane.

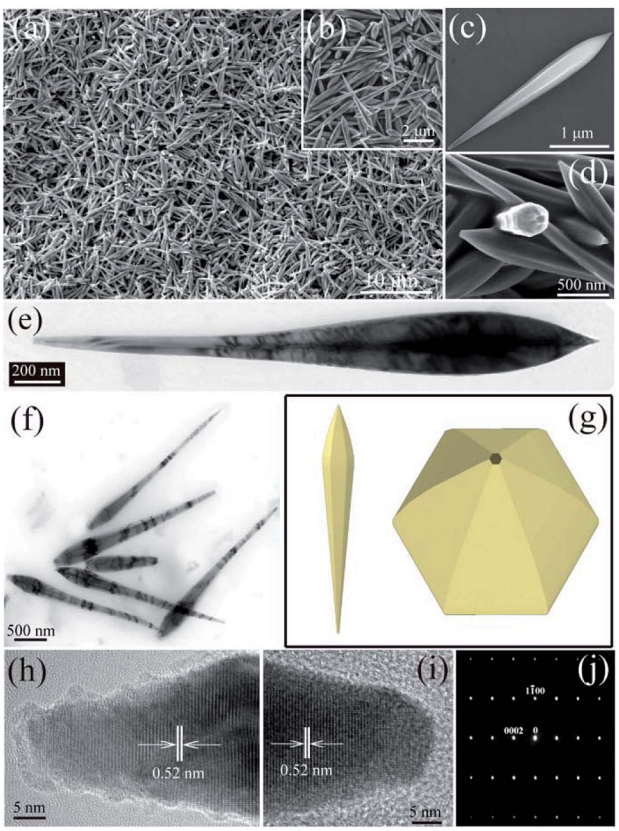

Fig. 2 Typical SEM and TEM images of the products generated at 330 °C and 17.2 MPa in hexane. (a)–(c) SEM images of the ZnO nanospindles. (d) A top view SEM image of the ZnO nanospindles. (e) and (f) TEM images of nanospindles. (g) Illustrations of a ZnO nanospindle viewed from the side and an end. (h) and (i) HRTEM images of two tips from a single nanospindle and (j) its corresponding SAED pattern.

Si substrates. The TEM and SEM images of the products (Fig. 2c–f) show a unique spindle-like shape with two sharp tips at different degrees of tapering angle (thinning) and six well-defined crystallographic facets along the *c* axis of each nanospindle. The side and top view of the ZnO nanospindle can be described by the drawing shown in Fig. 2g. The cross-section of the nanospindles is hexagonal. Fig. 2h and i show high-resolution TEM (HRTEM) images of the two tips that are only a few nanometers in size at the thinner (Fig. 2h) and the thicker end (Fig. 2i). The lattice spacing at 0.52 nm corresponds to the (0001) crystal plane of the wurtzite ZnO, indicating that the ZnO nanospindles grow along the *c* axis, which is consistent with 1D ZnO growth.[46] The corresponding SAED pattern (Fig. 2j) of the ZnO nanospindles shows a set of well-defined spots that confirm the single crystallinity of the products; it can be indexed as a hexagonal ZnO growth along the ⟨0001⟩ direction. ZnO nanocrystals are reported to minimize the polar (0001)-Zn plane and (000-1)-O plane under certain conditions.[47,48] Our TEM analysis also shows a similar result. According to TEM, SEM and XRD analyses (Fig. S1–S3†), the shape and morphology of the ZnO nanospindles can be characterized as a wurtzite structure of ZnO nanospindles with micrometer length growth along the *c* axis (⟨0001⟩ direction) with a curved surface and diameters ranging from 320–480 nm in the thickest part to 8–40 nm around the tips with a different tapering rate.

An interesting phenomenon is often observed when we use TEM to analyze the ZnO nanospindles. A dark contrasting line appears, running the entire length of the nanospindles in the zero-beam bright field image, representing the evidence for a screw dislocation, which is consistent with previous reports.[49–51] Although it is well-known that dislocations are mobile, instable and have a small volume, implying that they may move out from the crystals during the growth process or TEM sample preparation, the screw dislocation may also be stable even in 1-D nanomaterials due to an uniform twist caused by the elastic field of the dislocations.[52] To achieve a better picture of the presence of screw dislocation in the ZnO nanospindles, we performed diffraction contrast TEM under two-beam conditions. To obtain the direction of dislocation Burgers vector, it is necessary to find two non-collinear diffraction vectors, which meet the invisibility criterion ($g\boldsymbol{b} = 0$, where $\boldsymbol{b}$ is the Burgers vector and g is the diffraction vector) while using the diffraction contrast TEM. Therefore, the direction of the dislocation Burger vector by the cross product of these two g vectors can be determined. As shown in Fig. 3a, the analysis area (tagged with a red rectangle) was tilted toward the [10-10] zone axis and [11-20] zone axis under the two-beam conditions, which can be described by the drawing shown in Fig. 3b and f, respectively. Electron diffraction patterns of the analysis area along the [10-10] zone axis and [11-20] zone axis are shown in Fig. 3c and g. When diffraction contrast images are obtained along the [10-10] zone axis, the contrast of the dislocation line becomes visible under the two-beam condition, which excites the (0002) diffraction spot (Fig. 3d, represents $g \| \boldsymbol{b}$ conditions), whereas the contrast of the dislocation becomes invisible, meeting the invisibility criterion with the (1-210) diffraction spot (Fig. 3e). Similarly, the same results were

 This journal is © The Royal Society of Chemistry 2014

Published on 23 May 2014. Downloaded by National Tsing Hua University on 13/08/2015 11:50:24.

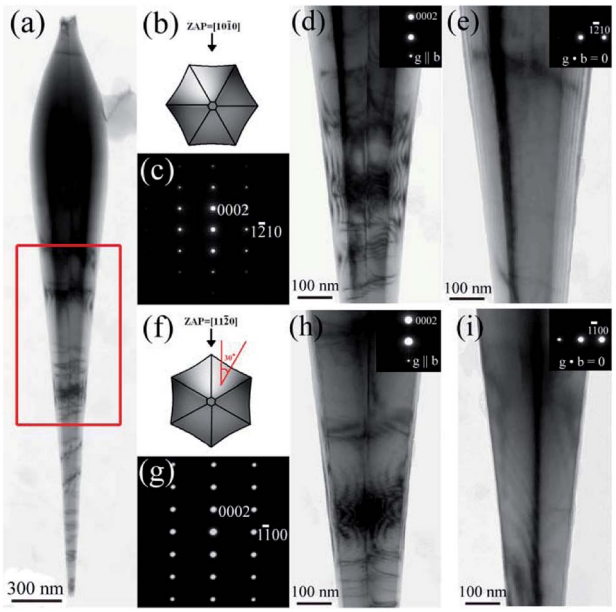

Fig. 3 (a) TEM image of a single ZnO nanospindle; the analyzed area was tagged with red rectangle and tiled to [10-10] and [11-20] zone axis. (b) and (f) Schematic diagrams of the zone axis were viewed under two beam conditions and (c) and (g) their corresponding SAED patterns, respectively. (d) and (e) Diffraction contrast TEM images viewed along the [10-10] zone axis with the (0002) diffraction spot and (1-210) diffraction spot. (h) and (i) Diffraction contrast TEM images viewed along the [11-20] zone axis with the (0002) diffraction spot and (1-100) diffraction spot.

observed in the diffraction contrast images obtained along the [11-20] zone axis when exciting the (0002) diffraction spot (Fig. 3h); the dislocation line becomes visible, whereas the dislocation line becomes invisible (Fig. 3i) when exciting the (1-100) diffraction spot. Therefore, the dislocation Burgers vector (b) is determined along the [0002] direction by taking the cross product of the two g vectors, (1-210) and (1-100), which is the same direction of the growth axis of ZnO nanospindles. Fig. 4 also shows a bright-field image recorded along [10-10] zone axis at the thick end of the ZnO nanospindle, corresponding to the dark-field image on the same region with the (000-2) diffraction spot, where a distinct white-contrasted dislocation line is visible in the dark-field TEM image. This also confirms that only one dislocation line is present in the nanospindle.

In addition, the apparent protrusion that exists on the ends in some ZnO nanospindles under TEM characterization was observed. Fig. 5b shows the TEM image of the tips (tagged with red circles) from the ZnO nanospindle, as shown in Fig. 5a. Based on the abovementioned analysis (Fig. 1, TEM characterization), the tip at the thinner end of the ZnO nanospindles is the [0002] end and exhibits protrusion features at the edge of ZnO nanospindles. We deduced that the protrusion on the end was produced by spiral growth steps at the tips of the nanospindles, which can also be regarded as a characteristic of dislocations.[38,42] Fig. 5c shows more clearly the spiral growth steps on the [0002] end, and its corresponding illustration is shown in Fig. 5d. It is well-known that the dislocation can be introduced into crystals if supersaturation in the system is high. We believe that the dislocations were introduced in the initial stage of the reactions due to relatively high supersaturation. When dislocation is introduced, it provides active sites for crystal growth. The driving force for crystal growth driven by dislocation spiral growth steps can not be avoided, even at relatively high supersaturation during the initial stage of the reaction. The emergent spiral growth steps on the ends of nanospindles can act as permanent self-perpetuating step sources, permitting the crystal growth of c axis to occur during the entire reaction.

To investigate the growth process of the ZnO nanospindles, we carried out a series of control experiments at a fixed temperature (330 °C) and molar injection rate (0.03 mmol min^{-1}) but at different reaction time intervals. Fig. 6b shows the hexagonal disc-like crystallites with diameters ranging from 85–150 nm, which were formed at a reaction time of 2.5 min. We deduce that the hexagonal discs are created by ultra-small ZnO

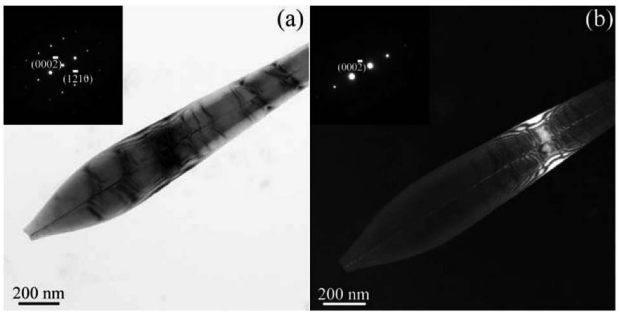

Fig. 4 (a) A bright field image of a single ZnO nanospindle with black contrast screw dislocation line at a thicker region taken from the [10-10] zone axis; and (b) the corresponding dark field image of the same nanospindle with a white contrast screw dislocation line exciting the (0002) diffraction spot under a two-beam condition.

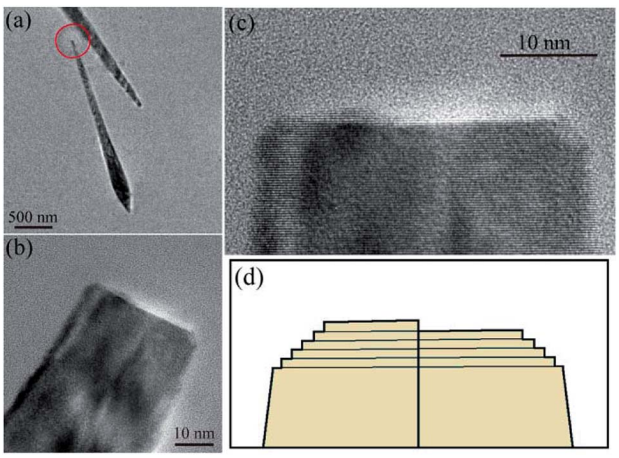

Fig. 5 (a) Low-magnification TEM image of ZnO nanospindles prepared at 330 °C; (b) TEM image of [0002] end from the same nanospindle shown in (a) and tagged with red circle; (c) TEM image of the [0002] end from the nanospindle shown in (b) and (d) the corresponding illustration of its spiral step.

Published on 23 May 2014. Downloaded by National Tsing Hua University on 13/08/2015 11:50:24.

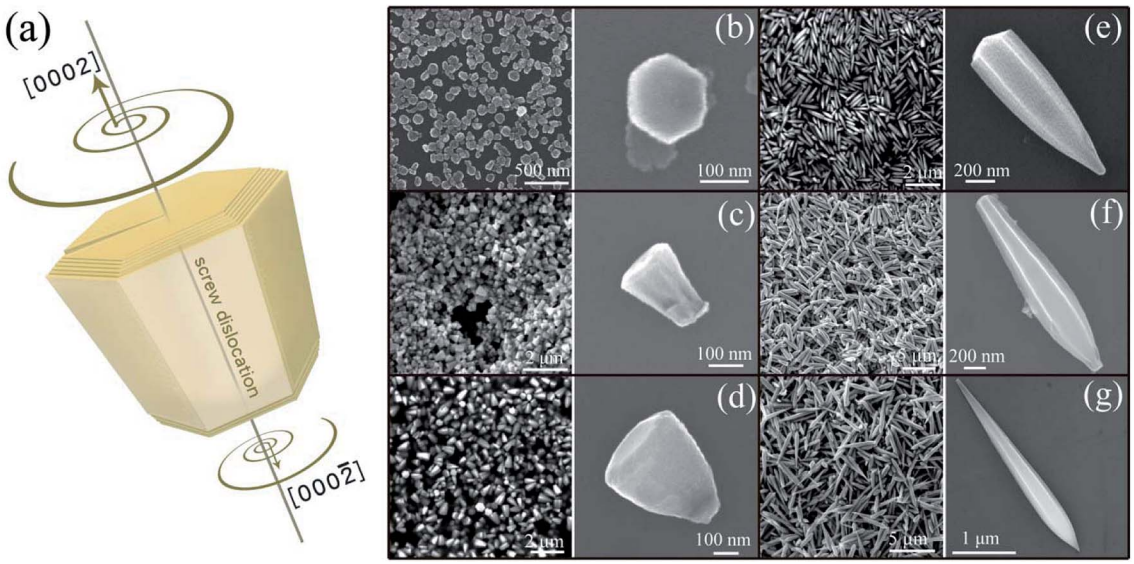

Fig. 6 (a) Illustration of the ZnO nanospindles driven by a combined growth consists of screw dislocation and LBL deposition. SEM images of the products obtained at the same reaction temperature (330 °C) and molar injection rate (0.03 mmol min^{-1}) but different reaction time intervals of (b) 2.5 min, (c) 10 min, (d) 12.5 min, (e) 22.5 min, (f) 30 min, and (g) 40 min.

particles or nuclei, which are produced *via* nucleophilic addition/elimination processes. The hexagonal discs exhibit a polar zinc (0001) face, six symmetric nonpolar {10-10} planes, and a polar oxygen (000-1) face, which is similar to its hexagonal close packing unit cell. In accordance with TEM characterization (Fig. 7), the hexagonal discs are single crystalline with a (0001) plane for one face and a (000-1) plane for the other face. The hexagonal disc seeds for further nanospindle growth should contain some defects, such as dislocations, which are probably generated because of slight misorientation by imperfectly oriented attachment at the beginning of the reaction.[53] When the reaction time was increased to 10–12.5 minutes, the nanodisc grew along the ⟨0002⟩ direction with one end [0002] getting thicker and the other [000-2] getting thinner. Half-nanospindles were formed at this time, as shown in Fig. 6c and d. With reaction time increased to 22.5–40 min (as shown in Fig. 6e–g), both ends also became thinner but the growth rate of the [0002] was significantly larger than the [000-2] end.

ZnO is a polar crystal in nature.[54,55] A convergent beam election diffraction (CBED) measurement was used to determine the polarity of the ZnO nanospindles. Fig. 8b and e show an experimental CBED pattern obtained from the red circle area of a ZnO half-nanospindle (Fig. 8a) and nanospindle (Fig. 8d) viewed along the [01-10] zone axis, respectively. The intensity distributions in the (0002) and (000-2) diffraction discs are quite different due to the wurtzite structure of ZnO.[56] Fig. 8c and f show the simulated CBED patterns using 100 nm and 205 nm as the ZnO thickness, respectively. By comparing the experimental and simulated CBED patterns, a good match between the experimental and simulated CBED results indicates that the

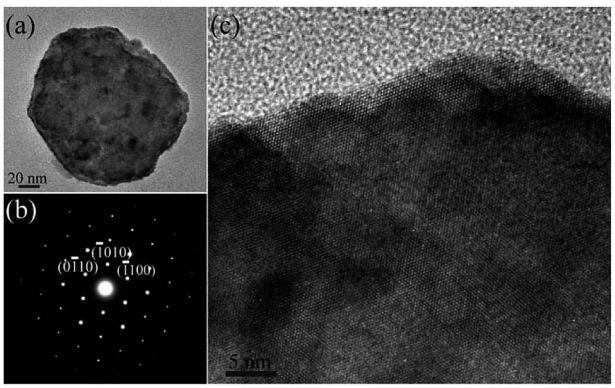

Fig. 7 (a) TEM image of a single ZnO nanodisk prepared at 330 °C, molar injection rate of 0.03 mmol min^{-1} and 2.5 min reaction time, and its corresponding (b) SAED pattern and (c) HRTEM image recorded from the [0001] zone axis.

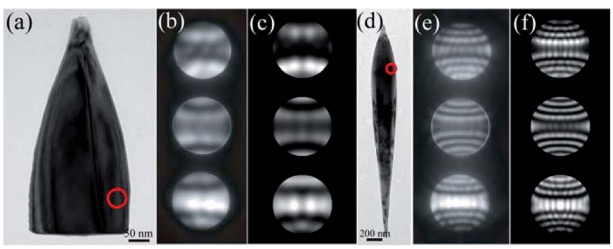

Fig. 8 (a) TEM image of a single ZnO semi-nanospindle; the analyzed area is tagged with a red circle. (b) Experimental CBED pattern obtained from the circle area of the half-nanospindle and recorded along the [10-10] zone axis. (c) Simulated CBED pattern at a thickness of 100 nm. (d) TEM image of a single ZnO nanospindle; the analyzed area is tagged with a red circle. (e) Experimental CBED pattern obtained from the circle area of the nanospindle and recorded along the [10-10] zone axis. (f) Simulated CBED pattern at a thickness of 205 nm.

This journal is © The Royal Society of Chemistry 2014

Published on 23 May 2014. Downloaded by National Tsing Hua University on 13/08/2015 11:50:24.

ZnO nanospindles with a thinner and thicker end grow with a (0001)-Zn polar surface and a (000-1)-O polar surface, respectively. The sequences of the growth velocities of ZnO crystals in different directions are [0001] > [01-1-1] > [01-10] > [01-11] > [000-1] under hydrothermal conditions, and the ratio of growth rates between the fast [0001] and slow [000-1] direction was 3 : 1.[57] Therefore, the growth rate at [0001] should be greater than that at [000-1], which is consistent with our experimental results. Finally, the asymmetry nanospindles were obtained at 40 min.

The sizes and aspect ratios of the ZnO nanospindles at different reaction time intervals are summarized in Table 1. The diameter of the ZnO nanocrystals was measured at the thickest region. First, in the early stage (10 to 22.5 min), the average diameter increased from 0.27 to 0.37 μm, and the length of the nanospindles increased from 0.37 to 1.17 μm. In the following interval of 22.5 min to 40 min, the average diameter increased from 0.37 to 0.44 μm and the spindle length increased from 1.17 to 3.78 μm. From statistics, the axial growth rate is always greater than the radial growth rate. Moreover, the axial growth rate gradually increased from 64 nm min^{-1} (10–22.5 min) to 149 nm min^{-1} (22.5–40 min), whereas the radial growth rate decreased from 8 nm min^{-1} (10–22.5 min) to 4 nm min^{-1} (22.5–40 min). This shows that the radial growth rate is more obvious in the earlier stage (note: the nanodiscs were mainly generated before 10 min of reaction time).

According to the classical crystal growth theory,[58] supersaturation dominates the model of crystal growth, which can be divided into three distinctive growth regimes: dislocation-driven growth, LBL growth, and dendritic growth. Dislocation-driven growth tends to occur when supersaturation is sufficiently low, whereas LBL is favoured when supersaturation is high. To trigger the dislocation-driven growth, two conditions must be satisfied: the presence of dislocation sources and low precursor supersaturation.[38,49,59,60] We must point out that in our system, supersaturation is related to the molar injection rate and the precursor decomposition rate in the reaction. In addition, the molar injection rate and the concentration of ZnO monomers in the reactor changed during the course of the reaction time: the precursor concentration in the 10 mL injection loop was gradually diluted by the incoming hexane, and the monomers in the reactor also depleted with time. Therefore, we can understand that the disc-like products are obtained at 2.5 min due to the high supersaturation in the initial stage. It is well-known that high supersaturation tends to spontaneously generate defects[61] such as dislocation. The dislocation sources have been introduced at this time. The following crystal growth not only occur along the *c*-axis due to the existence of dislocation seeds but also along the *a* and *b*-axis because the degree of supersaturation is still high in the reactor. Sears *et al.* also observed that mercury whiskers thicken radially when the mercury pressure (supersaturation) is increased.[62] Therefore, the driving forces of crystal growth along the *c* axis were dominated by dislocation growth but for the *a* and *b* axis, the driving forces of crystal growth should be dominated by the LBL mechanism because only one dislocation line is observed along the *c* axis. Afterward, the molar injection rate and the degree of supersaturation gradually decreased. Hence, the driving forces of LBL growth for the *a* and *b* axis gradually decreased (reducing the diameter) and dislocation-driven growth gains have more influence on the *c* axis (increasing the growth rate of the *c* axis) after about 22.5 minutes. The tapering phenomenon of ZnO was caused by a gradually decreased supply of growth resource.[63] Morin *et al.* also showed a steady decrease in the diameter of 1-D ZnO nanomaterials when continuous flow reactors are operated at decreasing precursor concentrations;[38] therefore, the gradual decrease in supersaturation is responsible for the gradual decrease in diameter (tapering).[64] Finally, the asymmetry nanospindles with two sharp tips and different degrees of tapering were obtained after 40 min. Fig. 6a also shows an illustration of the growth of asymmetrical axial ZnO nanospindles.

In addition, we studied the effect of precursor concentration on the synthesis. A parallel experiment was carried out in which the initial concentrations of $Zn(Ac)_2$–OLA complex were increased from 0.03 to 0.72 mmol min^{-1} while other experimental conditions remained constant. In this case, the reaction environment was always maintained at a high supersaturation state due to the high molar injection rate. Fig. 9 shows the SEM and TEM images of the products with typical rod shapes composed of well-defined {10-10} and (000-1) and {10-11} surfaces obtained under this high supersaturation condition. The growth is very consistent with the ZnO crystal obtained by the hydrothermal method.[57] Higher initial concentration of $Zn(Ac)_2$–OLA complexes implies that more ZnO monomers are produced, which in turn induce significant LBL growth; consequently, the driving forces of crystal growth by dislocation should be significantly inhibited. According to our statistical results, the average length of nanorods (435 nm) is shorter than that of nanospindles (3.78 μm). This implies that the axial growth is reduced due to the high supersaturation condition.

Table 1 Summary of the ZnO nanostructures obtained with different reaction time

Reaction time (min)	10	12.5	22.5	30	40
Average diameter in the thickest part (μm)	0.27	0.35	0.37	0.43	0.44
Average length (μm)	0.37	0.65	1.17	2.71	3.78

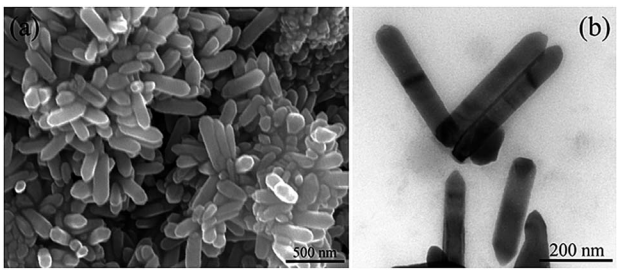

Fig. 9 (a) SEM and (b) TEM images of ZnO nanorods fabricated at a high molar injection rate of 0.72 mmol min^{-1} with reaction time of 40 min at 330 °C.

Published on 23 May 2014. Downloaded by National Tsing Hua University on 13/08/2015 11:50:24.

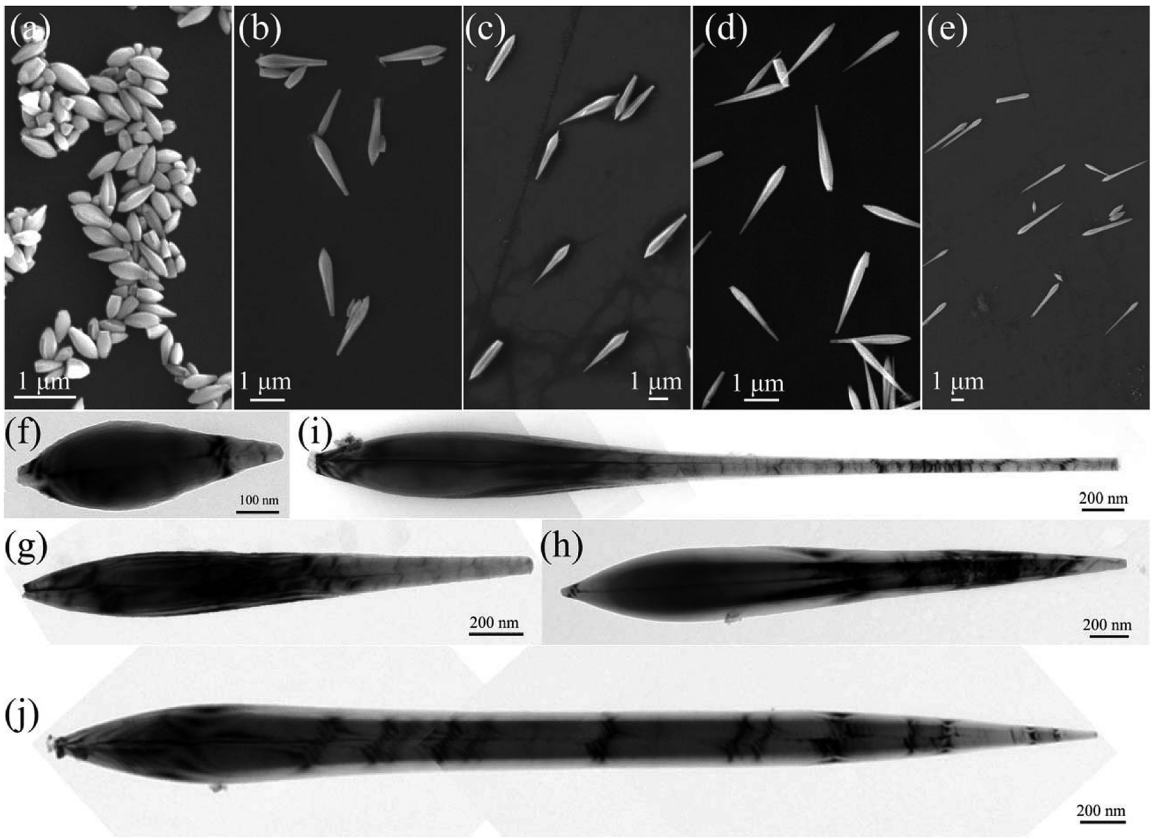

Fig. 10 SEM and TEM images of the ZnO nanospindles synthesized at the same molar injection rate (0.03 mmol min^{-1}) and reaction time (40 min) at different reaction temperatures of: (a) and (f) 270 °C, (b) and (g) 290 °C, (c) and (h) 310 °C, (d) and (i) 330 °C, (e) and (j) 370 °C.

We observed that the axial growth rate of ZnO nanospindles driven by screw dislocation is proportional to the reaction temperature. A series of control experiments were performed by changing the reaction temperature. SEM images and the corresponding TEM images of ZnO nanospindles synthesized at 40 min reaction time but different temperature intervals of 270 °C, 290 °C, 310 °C, 330 °C, and 370 °C are shown in Fig. 10. The lengths of the products were 0.62 μm, 1.87 μm, 2.98 μm, 4.05 μm, and 4.74 μm as the reaction temperature increased. The screw dislocation lines are also present. Although the thickness of the nanospindles increases from ~200 nm to 360 nm at elevated temperatures, the growth rate of length (*c* axis) for the nanospindles is significantly faster than that along the *a* axis of ZnO. It is similar for the dislocation-driven growth of PbS nanowire pine trees, where the length of the pine trees (trunk) increase as the temperature is elevated.[36] The present results show that length-tunable asymmetrical axial ZnO nanospindles are thermally controllable by varying the reaction temperature.

Conclusions

Asymmetrical axial ZnO nanospindles were synthesized *via* a non-hydrolytic method by the decomposition of zinc acetate at supercritical hexane environment. For the specific case of ZnO nanospindles, dislocations are spontaneously generated because of high supersaturation in the initial stage of the reaction, and the following crystal growth for *c* axis is mainly driven by dislocations; the LBL mechanism accounts for *a* and *b* axis. Afterward, the driving forces of crystal growth became gradually more pronounced by dislocation growth and debilitated by LBL growth when the supersaturation level started to decline. Moreover, a wide range of length (or aspect ratio) of ZnO nanospindles can be tuned by the temperature-mediated growth. Therefore, the final morphologies depend on the competition between these two growth modes.

Acknowledgements

The authors acknowledge the financial support by the Ministry of Science and Technology of Taiwan (NSC 102-2221-E-007-023-MY3, NSC 102-2221-E-007-090-MY2, NSC 101-2623-E-007-013-IT, and NSC 102-2633-M-007-002), the Ministry of Economic Affairs, Taiwan (101-EC-17-A-09-S1-198), National Tsing Hua University (102N2051E1, 102N2061E1), and the assistance from Center for Energy and Environmental Research, National Tsing-Hua University.

Notes and references

1 F. Shieh, A. E. Saunders and B. A. Korgel, *J. Phys. Chem. B*, 2005, **109**, 8538–8542.
2 Y. Sun and Y. Xia, *Science*, 2002, **298**, 2176–2179.

 This journal is © The Royal Society of Chemistry 2014

Published on 23 May 2014. Downloaded by National Tsing Hua University on 13/08/2015 11:50:24.

3 J. Park, J. Joo, S. G. Kwon, Y. Jang and T. Hyeon, *Angew. Chem., Int. Ed.*, 2007, **46**, 4630–4660.
4 M.-Y. Chiang, S.-H. Chang, C.-Y. Chen, F.-W. Yuan and H.-Y. Tuan, *J. Phys. Chem. C*, 2011, **115**, 1592–1599.
5 X. Lu, M. Yavuz, H.-Y. Tuan, B. A. Korgel and Y. Xia, *J. Am. Chem. Soc.*, 2008, **130**, 8900–8901.
6 H.-Y. Tuan, D. C. Lee, T. Hanrath and B. A. Korgel, *Chem. Mater.*, 2005, **17**, 5705–5711.
7 R. Brayner, S. A. Dahoumane, C. Yepremian, C. Djediat, M. Meyer, A. Coute and F. Fievet, *Langmuir*, 2010, **26**, 6522–6528.
8 G. Ma, Y. Zhou, X. Li, K. Sun, S. Liu, J. Hu and N. A. Kotov, *ACS Nano*, 2013, **7**, 9010–9018.
9 Z. Tang, Z. Zhang, Y. Wang, S. C. Glotzer and N. A. Kotov, *Science*, 2006, **314**, 274–278.
10 A. P. LaGrow, S. Cheong, J. Watt, B. Ingham, M. F. Toney, D. A. Jefferson and R. D. Tilley, *Adv. Mater.*, 2013, **25**, 1552–1556.
11 J. Watt, C. Yu, S. L. Y. Chang, S. Cheong and R. D. Tilley, *J. Am. Chem. Soc.*, 2013, **135**, 606–609.
12 X. Lu, M. Rycenga, S. E. Skrabalak, B. Wiley and Y. Xia, *Annu. Rev. Phys. Chem.*, 2009, **60**, 167–192.
13 R. Jin, Y. C. Cao, E. Hao, G. S. Métraux, G. C. Schatz and C. A. Mirkin, *Nature*, 2003, **425**, 487–490.
14 P. Yang, R. Yan and M. Fardy, *Nano Lett.*, 2010, **10**, 1529–1536.
15 F.-W. Yuan, H.-J. Yang and H.-Y. Tuan, *ACS Nano*, 2012, **6**, 9932–9942.
16 H.-J. Yang, S.-Y. He and H.-Y. Tuan, *Langmuir*, 2014, **30**, 602–610.
17 P. R. Chalker, P. A. Marshall, P. J. King, K. Dawson, S. Romani, P. A. Williams, J. Ridealgh and M. J. Rosseinsky, *J. Mater. Chem.*, 2012, **22**, 12824–12829.
18 K. R. Raghupathi, R. T. Koodali and A. C. Manna, *Langmuir*, 2011, **27**, 4020–4028.
19 C. Battaglia, J. Escarré, K. Söderström, M. Charrière, M. Despeisse, F.-J. Haug and C. Ballif, *Nat. Photonics*, 2011, **5**, 535–538.
20 R. Agrawal and H. D. Espinosa, *Nano Lett.*, 2011, **11**, 786–790.
21 K. H. Müller, J. Kulkarni, M. Motskin, A. Goode, P. Winship, J. N. Skepper, M. P. Ryan and A. E. Porter, *ACS Nano*, 2010, **11**, 6767–6779.
22 H. Yan, R. He, J. Pham and P. Yang, *Adv. Mater.*, 2003, **15**, 402–405.
23 S. Kar, B. N. Pal, S. Chaudhuri and D. Chakravorty, *J. Phys. Chem. B*, 2006, **110**, 4605–4611.
24 S. Ashraf, A. C. Jones, J. Bacsa, A. Steiner, P. R. Chalker, P. Beahan, S. Hindley, R. Odedra, P. A. Williams and P. N. Heys, *Chem. Vap. Deposition*, 2011, **17**, 45–53.
25 Z. Wang, X. F. Qian, J. Yin and Z. K. Zhu, *Langmuir*, 2004, **20**, 3441–3448.
26 B. Liu and H. C. Zeng, *J. Am. Chem. Soc.*, 2003, **125**, 4430–4431.
27 M. J. Zheng, L. D. Zhang, G. H. Li and W. Z. Shen, *Chem. Phys. Lett.*, 2002, **363**, 123–128.
28 N. S. Ramgir, K. Subannajui, Y. Yang, R. Grimm, R. Michiels and M. Zacharias, *J. Phys. Chem. C*, 2010, **114**, 10323–10329.
29 L. C. Campos, M. Tonezzer, A. S. Ferlauto, V. Grillo, R. Magalhães-Paniago, S. Oliveira, L. O. Ladeira and R. G. Lacerda, *Adv. Mater.*, 2008, **20**, 1499–1504.
30 H. Yoon, K. Seo, H. Moon, K. S. K. Varadwaj, J. In and B. Kim, *J. Phys. Chem. C*, 2008, **112**, 9181–9185.
31 G. Shen, P. C. Chen, K. Ryu and C. Zhou, *J. Mater. Chem.*, 2009, **19**, 828–839.
32 H. T. Ng, J. Han, T. Yamada, P. Nguyen, Y. P. Chen and M. Meyyappan, *Nano Lett.*, 2004, **4**, 1247–1252.
33 P.-H. Yeh, Z. Li and Z. L. Wang, *Adv. Mater.*, 2009, **21**, 4975–4978.
34 D. Vanmaekelbergh and L. K. van Vugt, *Nanoscale*, 2011, **3**, 2783–2800.
35 G. W. Sears, *Acta Metall. Mater.*, 1955, **3**, 367–369.
36 M. J. Bierman, Y. K. A. Lau, A. V. Kvit, A. L. Schmitt and S. Jin, *Science*, 2008, **320**, 1060–1063.
37 H. Y. Wu, F. Meng, L. S. Li, S. Jin and G. F. Zheng, *ACS Nano*, 2012, **6**, 4461–4468.
38 S. A. Morin, M. J. Bierman, J. Tong and S. Jin, *Science*, 2010, **328**, 476–480.
39 F. Meng, S. A. Morin and S. Jin, *J. Am. Chem. Soc.*, 2011, **133**, 8408–8411.
40 Y. K. A. Lau, D. J. Chernak, M. J. Bierman and S. Jin, *J. Am. Chem. Soc.*, 2009, **131**, 16461–16471.
41 D. Maestre, D. Haussler, A. Cremades, W. Jager and J. Piqueras, *J. Phys. Chem. C*, 2011, **115**, 18083–18087.
42 J. Zhu, H. L. Peng, A. F. Marshall, D. M. Barnett, W. D. Nix and Y. Cui, *Nat. Nanotechnol.*, 2008, **3**, 477–481.
43 X. Han, X. Zhou, Y. Jiang and Z. Xie, *J. Mater. Chem.*, 2012, **22**, 10924–10928.
44 S. Hacialioglu, F. Meng and S. Jin, *Chem. Commun.*, 2012, **48**, 1174–1176.
45 Z. H. Zhang, M. H. Lu, H. R. Xu and W. S. Chin, *Chem.–Eur. J.*, 2007, **13**, 632–638.
46 Z. L. Wang, X. Y. Kong and J. M. Zuo, *Phys. Rev. Lett.*, 2003, **91**, 185502.
47 M. Yang, K. Sun and N. A. Kotov, *J. Am. Chem. Soc.*, 2010, **132**, 1860–1872.
48 Z. L. Wang, *J. Phys.: Condens. Matter*, 2004, **16**, R829–R858.
49 S. Jin, M. J. Bierman and S. A. Morin, *J. Phys. Chem. Lett.*, 2010, **1**, 1472–1480.
50 Q. M. Li, Y. Lin, J. R. Creighton, J. J. Figiel and G. T. Wang, *Adv. Mater.*, 2009, **21**, 2416–2420.
51 Y. G. Li and Y. Y. Wu, *Chem. Mater.*, 2010, **22**, 5537–5542.
52 J. D. Eshelby, *J. Appl. Phys.*, 1953, **24**, 176–179.
53 R. L. Penn and J. F. Banfield, *Science*, 1998, **281**, 969–971.
54 S. K. Hong, H. J. Ko, Y. F. Chen and T. Yao, *J. Vac. Sci. Technol., B: Microelectron. Nanometer Struct.–Process., Meas., Phenom.*, 2002, **20**, 1656–1663.
55 P. W. Tasker, *J. Phys. C: Solid State Phys.*, 1979, **12**, 4977–4984.
56 Z. L. Wang, *J. Phys. Chem. B*, 2000, **104**, 1153–1175.
57 W. J. Li, E. W. Shi, W. Z. Zhong and Z. W. Yin, *J. Cryst. Growth*, 1999, **203**, 186–196.
58 W. K. Burton, N. Cabrera and F. C. Frank, *Philos. Trans. R. Soc., A*, 1951, **243**, 299–358.

59 F. Meng, S. A. Morin, A. Forticaux and S. Jin, *Acc. Chem. Res.*, 2013, **46**, 1616–1626.
60 S. A. Morin and S. Jin, *Nano Lett.*, 2010, **10**, 3459–3463.
61 F. C. Frank, *Adv. Phys.*, 1952, **1**, 91–109.
62 G. W. Sears, *Acta Metall.*, 1955, **3**, 361–366.
63 P. A. Hu, Y. Q. Fu, L. Liu, X. B. Wang and D. B. Zhu, *Appl. Phys. A*, 2005, **80**, 35–38.
64 Z. W. Liang, H. Cui, K. Wang, P. H. Yang, L. Zhang, W. J. Mai, C. X. Wang and P. Y. Liu, *CrystEngComm*, 2012, **14**, 1723–1728.

Published on 23 May 2014. Downloaded by National Tsing Hua University on 13/08/2015 11:50:24.

This journal is © The Royal Society of Chemistry 2014